ADVANCED FUNCTIONAL MATERIALS
www.afm-journal.de

A Small Molecular Cathode for High-Performance Calcium Metal Batteries

*Yiyuan Ma, Qi Qi, Qi Meng, Yuyang Yi, Huijun Lin, Jingya Yu, Chi Fai Cheung, and Zheng-Long Xu**

Calcium-ion batteries are emerging as a promising alternative to lithium-ion batteries by offering potential advantages in cost, affordability, and safety. However, the development of high-performance calcium batteries has been hindered by the lack of high-capacity cathodes. Here a small molecular organic cathode, 9,10-phenanthrenequinone (PQ), is reported which leverages the rapid enolization chemistry of multi-redox centers (C═O) and the flexible intermolecular structure for high performance. The PQ cathode demonstrates an impressive specific capacity of 250 mAh g^{-1} at 0.2 C for 200 cycles and superior rate capabilities. The robust performance of PQ cathodes is attributed to the mitigation of small molecule electrode dissolution in the weakly solvating ether electrolytes and the promotion of inter-and intralayer Ca ion diffusion pathways, which synergistically facilitate the retention of high capacities at elevated current rates. When paired with a Ca metal anode, the full cell achieves remarkable capacities of 214 mAh g^{-1} at 0.2 C, with an average operating voltage of 2.5 V versus Ca/Ca^{2+}, representing the highest performance among CMBs reported to date. The use of organic cathodes in tailored electrolytes with restricted intermediate dissolutions heralds a new era in the development of multivalent metal batteries.

1. Introduction

Lithium-ion batteries (LIBs) have played an indispensable role in our society as energy storage solutions due to their high energy density, long cycle life, flexible design, and low self-discharge.[1] Nevertheless, the safety risks from lithium dendrite formation and the potential price spikes of lithium resources put the LIBs technology under widespread concerns as the principal power source for smart grids and e-transportation applications.[2] Alternative battery technologies that can provide better safety and affordability are therefore highly desirable. Among various contenders,[3] rechargeable calcium (Ca) batteries utilizing the divalent Ca^{2+} ions, stand out due to the fifth crustal abundance of Ca element and the possible dendrite-free deposition of high-capacity Ca metal anode (2072 mAh cm^{-3}), thus offering substantial improvements in affordability and safety of Ca metal batteries (CMBs). In addition, the Ca/Ca^{2+} redox potential of −2.87 V versus standard hydrogen electrode is close to that of Li/Li^+, suggesting possibly high-energy densities for CMBs.[4] The recent advancements in anode materials (i.e., Ca metal,[5] graphite) and nonaqueous electrolytes (i.e., $Ca(BH_4)_2$ in tetrahydrofuran (THF), $Ca[B(hfip)_4]_2$ in dimethoxyethane (DME)) have brought CMBs a step closer to practical realization. Nonetheless, the development of high-capacity cathode materials remains a significant hurdle.[6] The intercalation-type cathodes (i.e., V_2O_5, MoO_3,[7] Prussian blue analogs $MnFe(CN)_6$,[8] and polyanionic $Ca_xNa_{0.5}VPO_{4.8}F_{0.7}$)[9] often exhibit inferior capacities (<150 mAh g^{-1}) and poor rate capabilities, thus impeding the progress of the forthcoming CMBs technology.

The poor performance of intercalation-type transition-metal-based cathodes is fundamentally linked to the properties of Ca^{2+} ions. The relatively large ionic radius and divalent nature of Ca^{2+} result in sluggish intercalation kinetics in the rigid metal oxide hosts. Moreover, environmental concerns regarding the carbon footprint associated with the manufacturing of transition metal-based materials further question the sustainability of these cathodes for CMBs. In contrast, organic materials have emerged as promising alternatives for their potentially low cost, sustainability, and massive producibility.[10] More importantly, organic materials can offer a much more flexible framework to accommodate large guest ions, like Ca^{2+}, and their composition of light weight elements and abundant redox motifs enable high capacities exceeding 250 mAh g^{-1}. Investigations on several organic materials, including 5,7,12,14-pentacenetetrone

Y. Ma, Q. Qi, Q. Meng, Y. Yi, H. Lin, J. Yu, C. F. Cheung, Z.-L. Xu
State Key Laboratory of Ultraprecision Machining Technology
Department of Industrial and Systems Engineering
The Hong Kong Polytechnic University
Hung Hom, Hong Kong 999077, P. R. China
E-mail: zhenglong.xu@polyu.edu.hk
Z.-L. Xu
Research Institute for Advanced Manufacturing
The Hong Kong Polytechnic University
Hung Hom, Hong Kong 999077, P. R. China

The ORCID identification number(s) for the author(s) of this article can be found under https://doi.org/10.1002/adfm.202411715

DOI: 10.1002/adfm.202411715

(PT), covalent organic framework with multiple carbonyls (TB-COF)[11] in aqueous electrolytes and poly(anthraquinonyl sulfide) (PAQS),[12] polytriphenylamine (PTPAn)[13] in nonaqueous electrolytes, have demonstrated encouraging electrochemical performance. However, achieving energy densities of above 500 Wh kg^{-1} for CMBs remains elusive, primarily because of the limited voltage windows (<1.6 V) in aqueous electrolytes and the reduced capacities from redox-inactive backbones in polymers.[14]

To address these issues, the direct cycling of small molecular cathodes in nonaqueous electrolytes presents a promising avenue, considering their high capacities and low molecular weights. Unfortunately, the propensity for dissolution of most small molecule electrodes in nonaqueous electrolytes precipitates rapid capacity decay and poor cycle life, which severely obstacles their practical application. In addition, organic crystals may suffer lattice disorder during repeated gust-ion insertion and extraction, further causing adverse effects on electrochemical reversibility. Strategies to mitigate electrode dissolution, such as polymerization, host impregnation, interlayer insertion, and utilization of highly concentrated electrolytes or inorganic solid-state electrolytes, have been explored in Li-ion and Na-ion batteries[15] but remain underexplored for organic cathodes in CMBs. A comprehensive understanding of the interplay among the electrode dissolution, solvent species, and electrolyte structure also remains elusive, which are critical pieces of the puzzle in advancing CMBs.

Herein, this work proposes a two-pronged approach to achieve high-performance and stable CMBs using small molecular cathodes. First, we achieve high Ca ion storage capacity and elevated operating voltage by employing a conjugated carbonyl-based material, 9,10-phenanthrenequinone (PQ) as high-performance cathodes. Second, we restrict the electrode dissolution by designing a low-solubility-driven electrolyte, specifically the 2.5 M $Ca(TFSI)_2$ tetraethylene glycol dimethyl ether (TEGDME) solution. The effectiveness of both strategies is validated by cycling PQ//activated carbon (AC) half cells and PQ//Ca metal full cells in compatible electrolytes. The electrochemical results are compelling: PQ cathodes deliver a high capacity of 250 mAh g^{-1} at 0.2 C at a voltage of 2.1 V versus Ca/Ca^{2+} for 200 cycles in half cells and a high capacity of 214 mAh g^{-1} in Ca metal full cells. The enhanced electrochemical performance is attributed to the strategic selection of low-solubility-driven solvent as informed by a molecular electrostatic potential (MESP) indicator, in conjunction with the distinctive Ca^{2+} ion storage mechanism in PQ. It is revealed that Ca^{2+} ions can transfer through inter- and intra-layer pathways parallel to aromatic stacks for rapid enolization of the conjugated carbonyl groups during the calciation. These insights are expected to expedite the development of high-capacity organic cathodes for sustainable Ca metal batteries.

2. Results and Discussion

PQ was selected as a representative small molecular cathode material to demonstrate the Ca^{2+} ion storage capabilities by following a comparative analysis of possible cathode material candidates in terms of the theoretical capacities and the redox voltage (**Figure 1a**). Scanning electron microscopy (SEM) revealed the morphology of PQ as a brick-like shape with approximate dimensions of 20 µm × 5 µm (Figure 1b). Figure 1c illustrates the molecular structure of PQ composed of offset stacked individual PQ molecules, fostering π–π interactions between the aromatic rings of adjacent molecules (Figure S1, Supporting Information). These interactions play a significant role for the structural integrity and Ca ion storage of the PQ material.[16] The X-ray diffraction (XRD) profile in Figure 1d exhibits a series of distinct peaks at $2\theta = 11.09°, 12.01°, 13.72°, 17.16°, 19.59°, 20.88°, 24.19°$, and 27.42°, corresponding to the (001), (220), (120), ($\bar{1}\bar{2}1$), (320), (231), ($\bar{1}\bar{1}2$), ($\bar{2}\bar{2}2$), and (001) planes of PQ crystal (PDF No. 46–1927). Fourier-transform infrared (FTIR) and liquid chromatography nuclear magnetic resonance (NMR) spectroscopy collectively confirmed the presence of carbonyl groups (C=O) in PQ for Ca^{2+} ion storage (Figure 1e,f).

Prior to the electrochemical cycling of the PQ cathode in Ca-ion cells, the propensity for electrode dissolution in nonaqueous electrolytes, a long-lasting problem for organic electrodes, was evaluated. **Figure 2a** shows the optical images of PQ electrodes immersed in a series of 0.5 M $Ca(TFSI)_2$ electrolyte solutions with different solvents, including DME, diethylene glycol dimethyl ether (DEGDME), TEGDME, dimethylacetamide (DMAc), acetonitrile (ACN), tetrahydrofuran (THF), and ethylene carbonate/propylene carbonate (EC:PC). The degree of PQ electrode dissolution was observed to follow the sequence of EC: PC > ACN, DMAc>DME > THF > DEGDME, TEGDME. The lowest PQ dissolution degree in TEGDME-based electrolytes was also substantiated by the UV–vis spectroscopy, which exhibited the lowest absorption peak at ≈400 nm.

To understand the solvent-dependent PQ dissolution in $Ca(TFSI)_2$ electrolytes, we then conducted density functional theory (DFT) calculations.[17] The insets of Figure 2b show the molecular electrostatic potentials (MESP) of PQ and the solvents under consideration, which reflect the positive (in red color) and negative (in blue color) electrostatic distributions across the molecules. This analysis facilitates the parameterization of molecular polarities by examining the electrostatic potential difference ($V_{s,\,max} - V_{s,\,min}$), the mean electrostatic potential difference ($V_s^+ - V_s^-$),[18] and the molecular polarity index (MPI) (Table S1, Supporting Information).[19] $V_{s,\,max} - V_{s,\,min}$ represents the difference between the largest and lowest electrostatic potentials on the molecular surface, while $V_s^+ - V_s^-$ measures the average deviation between positive and negative electrostatic potentials in the region. A higher value of these parameters indicates increased molecular polarization. The MPI is defined as the average of the absolute electrostatic potential values on the molecular surface, serving as an indicator of polarity. Figure 2b summarizes these three parameters for PQ and the solvents. It shows that DMAc, ACN, THF, EC, and PC solvents present $V_{s,\,max} - V_{s,\,min}$, $V_s^+ - V_s^-$ and MPI within a 20% variance of these for PQ. In contrast, TEGDME shows deviations of 35.40, 22.63, and 30.21% from PQ for these parameters, respectively. According to the "like dissolves like" principle,[20] this discrepancy suggests a low solubility of PQ in TEGDME than the other solvents, aligning with our experimental observations. Further immersion tests of PQ electrodes in other solvents (i.e., dimethylsulfoxide DMSO, dimethylformamide DMF, ethyl methyl carbonate EMC, diethyl carbonate DEC, etc.) with varying polarities in Figure S2 (Supporting Information) further validate the predictive accuracy of our solvent selection indicator.

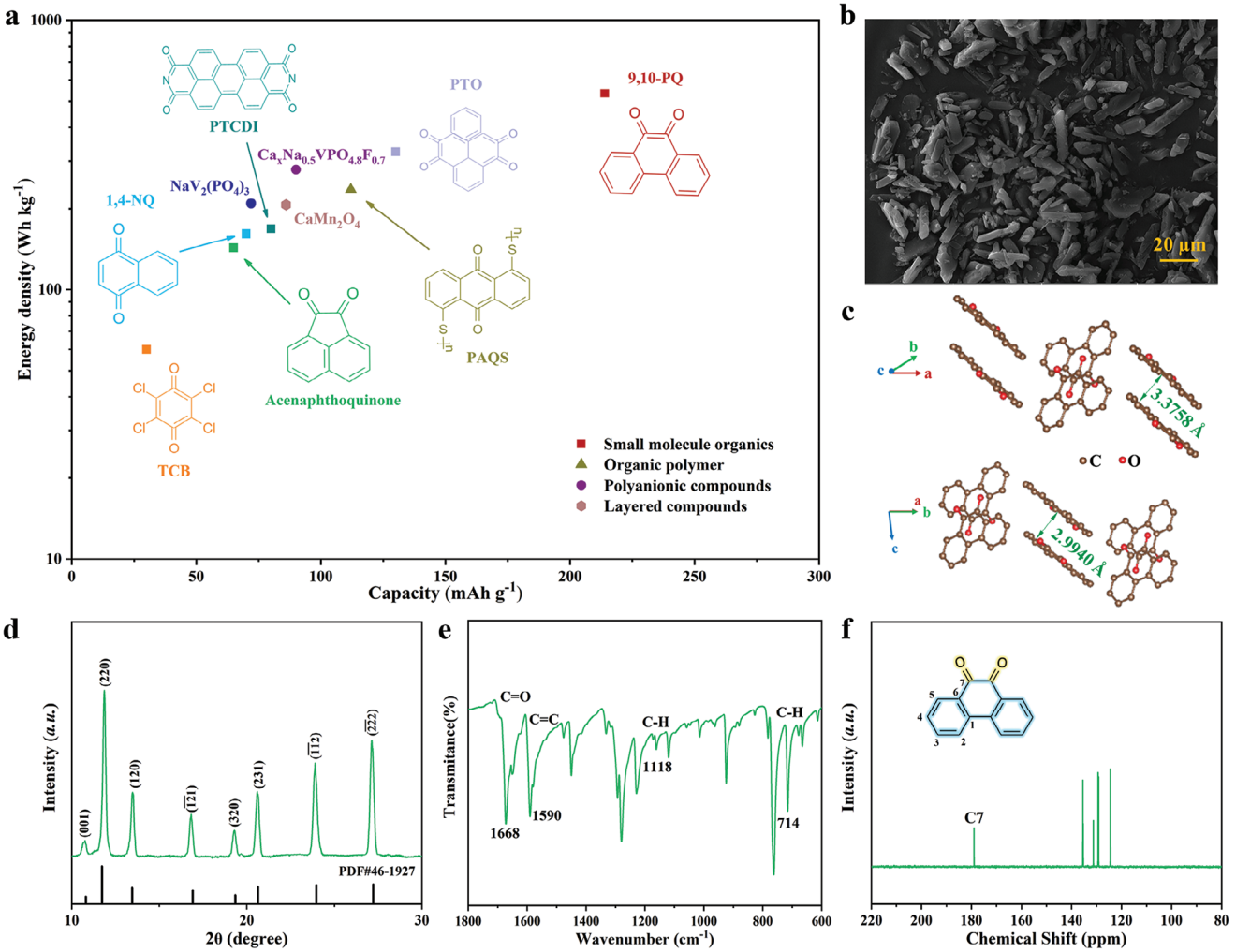

Figure 1. Morphology and structure characterization of the PQ materials. a) Capacities and energy densities of potential cathode materials, including organic materials, like 1,4-naphthalenedione (1,4-NQ), tetra-chloro-benzoquinone (TCB), pyrene-4,5,9,10-tetraone (PTO), 9,10-PQ, perylene tetracarboxylic diimide (PTCDI) and acenaphthoquinone, and polymer electrode PAQS,[12] inorganic compounds like $Ca_xNa_{0.5}VPO_{4.8}F_{0.7}$[9a] and $NaV_2(PO_4)_3$,[9b] layered compounds $CaMn_2O_4$.[7a] b) SEM image, c) schematic crystal structure, d) XRD pattern, e) FTIR spectrum, f) ^{13}C NMR of PQ material.

The electrochemical behaviors of PQ electrodes were then investigated by cyclic voltammetry (CV) scanning the Ca-ion half cells at 0.2 mV s^{-1} in 0.5 M $Ca(TFSI)_2$ dissolved in as-mentioned solvents. As shown in Figure 2c,d, the CV profiles display notable variations in redox peak positions and current densities. In the $Ca(TFSI)_2$ EC/PC electrolyte solution, PQ displayed two pairs of redox peaks at −0.44/−0.29 V and −1.07/−0.88 V versus activated carbon (AC) with diminishing peak intensities over cycles, indicative of substantial electrode dissolution in the EC/PC-based electrolyte. Notable is that the use of AC counter electrodes aims to exclude the complexity associated with the irreversibility of Ca metal electrodes in most organic electrolytes.[8a] Similar dissolution problems were also observed in the ACN and DME-based electrolytes. Despite the enhanced reversibility of PQ in DMAc, THF, and DME-based electrolytes, the low electrochemical activity (i.e., low peak currents in THF-based electrolytes) and poor reaction kinetics (i.e., large overpotentials in DMAc, DME, DEGDME-based electrolytes) rendered them unfavorable for PQ cathodes. In contrast, in the $Ca(TFSI)_2$ TEGDME electrolyte, PQ displayed high reversibility and stepwise enolizations with distinct redox pairs at −1.07/−0.90 V, −0.78/−0.72 V and −0.38/−0.37 V versus AC. The unique enolization process with three redox pairs is exclusively observed in Ca-ion systems (Figure S3, Supporting Information). This phenomenon may be attributed to the disproportionation of radical intermediates (PQ^-, PQ^--1/2 Ca^{2+}, and $PQ^{2-}Ca^{2+}$) or interactions between ortho-carbonyl groups and the electrolyte. A similar phenomenon has been observed with PTCDA in Ca-ion batteries.[21] It is noted that the redox peaks at −1.07/−1.09 V gradually diminishes after 4 cycles, possibly due to the activation and structural rearrangement of PQ electrodes. The minimal overpotentials for the dominant redox pairs (0.01–0.06 V) imply superior reaction kinetics of PQ in the TEGDME-based electrolyte. Further dissolution experiments on PQ electrodes revealed an inverse correlation with the TEGDME-based electrolyte concentrations (Figure S4, Supporting

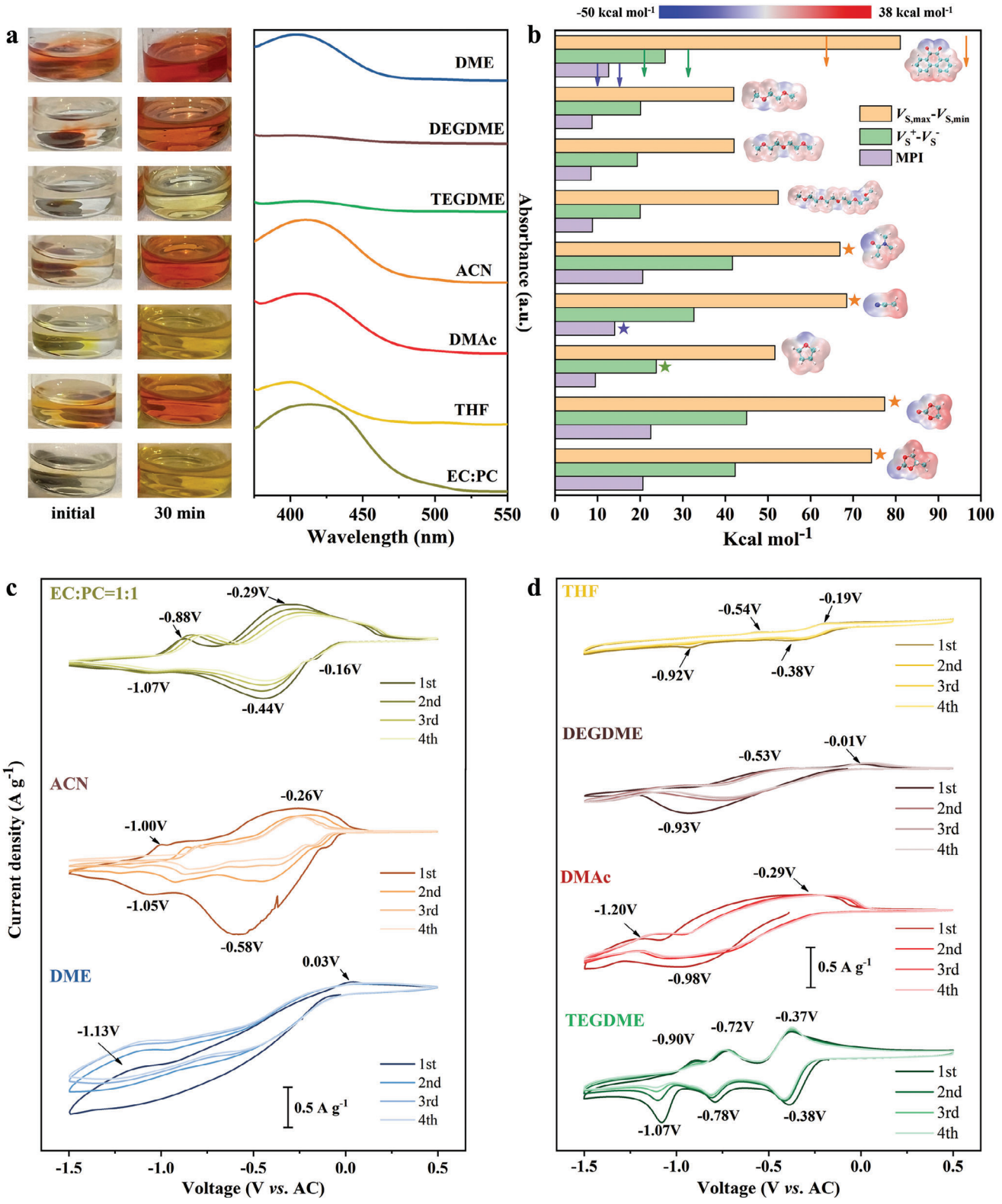

Figure 2. Low-solubility-driven non-aqueous electrolyte selection criteria for small molecular organic electrode. a) Optical photographs of PQ electrode soaking in various electrolytes for 30 min (left) and the corresponding UV–vis absorption spectra (right), b) calculated $V_{s,\,max} - V_{s,\,min}$, $V_s^+ - V_s^-$ and MPI parameters for PQ and solvents (Insets: MESP results of PQ and various solvents. The colored arrow ranges indicate the 20% similarity range of the related parameter, and the colored stars denote the solvents within this similarity range of the specific parameter. c,d) CV curves of PQ in the $Ca(TFSI)_2$-based electrolytes (inset c and d show the normalized current density scale).

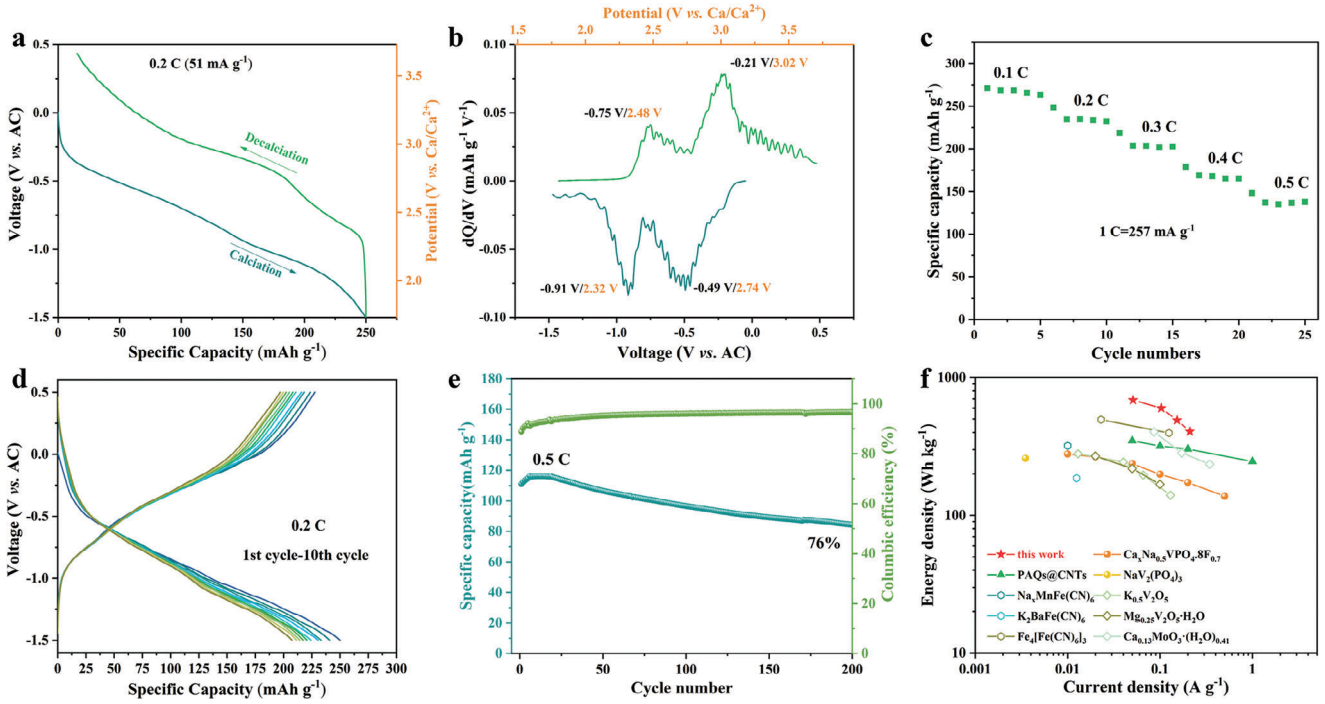

Figure 3. Electrochemical performance of PQ cathodes in Ca-ion half cells. a) Calciation/decalciation profiles of PQ in 2.5 M $Ca(TFSI)_2$/TEGDME electrolyte at 0.2 C, b) dQ/dV curves derived from (a) to show the redox peaks and calibrated voltages of PQ, c) specific capacities of PQ at current densities from 0.1 to 0.5 C. d) voltage profiles of PQ at 0.2 C over ten cycles, e) cyclic capacities and coulombic efficiencies of PQ at 0.5 C over 200 cycles, f) comparison of PQ with other cathodes for CIBs. See Table S2 (Supporting Information) for the detailed data of these cathode materials.

Information), justifying the necessity for additional measures, including concentrated electrolyte (i.e., 2.5 M $Ca(TFSI)_2$/TEGDME), graphene oxide interlayers to suppress shuttle effect[22] (Figure S5, Supporting Information) and carbon nanotube additive (Figure S6, Supporting Information) to improve conductivity, for further optimizing the electrochemical performance of PQ cathodes.

Galvanostatic discharging/charging profiles of PQ between −1.5 and 0.5 V versus AC (equivalent to 1.73–3.73 V versus Ca/Ca^{2+} as calibrated in Figure S7, Supporting Information) revealed an initial discharge capacity of 250 mAh g^{-1} (approximate 97.25% of the theoretical capacity) and a Coulombic efficiency of 93.83% (**Figure 3a**). The dQ/dV curves in Figure 3b identify two redox couples at −0.49/−0.75 V (2.74/2.48 V versus Ca/Ca^{2+}) and −0.91/−0.21 V (2.32/3.02 V versus Ca/Ca^{2+}), consistent with the distinguished plateaus in the discharge/charge profiles. Besides, a three-electrode test was performed for PQ to provide a more accurate assessment of the voltage range and reversible capacity (Figure S8, Supporting Information).[23] The capacities of the SWCNTs additive and GO interlayer were also measured in the Ca-ion system, which exhibited ≈8 and 0.5 mAh g^{-1} (Figure S9, Supporting Information), respectively. Therefore, the high capacity should be attributed to PQ active materials. The rate capability of PQ was evaluated at increasing current densities from 0.1 to 0.5 C (1 C = 257 mA g^{-1} corresponding to the current density for full calciation in 1 h) as shown in Figure 3c. PQ maintained discharge capacities of 261.4, 248.5, 218.8, 178.8, and 148.1 mAh g^{-1}, respectively, surpassing most of the transition-metal-based cathode materials.[7b,9b,24] Under deep discharging and charging at 0.2 C, the reversible capacity sustained above 200 mAh g^{-1} over 10 cycles (Figure 3d), in contrast to the abrupt capacity loss observed in other electrolytes (Figure S10, Supporting Information), emphasizing the critical role of solvent selection for PQ cathodes in Ca-ion batteries. When the PQ electrode was cycled at 0.5 C, 76% of the initial capacity could be maintained after 200 cycles along with an average Coulombic efficiency of ≈96% (Figure 3e), which far outperforms the cell performance in other inorganic cathodes or small molecule cathodes in literature (Table S2, Supporting Information). The specific energy density of PQ can be calculated to be 685 Wh kg^{-1} at 0.2 C based on the mass of active materials, which exceeds these for the state-of-the-art Ca-ion battery cathodes, including the 348 Wh kg^{-1} for PAQS,[14] 320 Wh kg^{-1} for $Na_xMnFe(CN)_6$,[8a] 278.4 Wh kg^{-1} for $Ca_xNa_{0.5}VPO_{4.8}F_{0.7}$,[9a] and 403 Wh kg^{-1} for $Ca_{0.13}MoO_3{\cdot}(H_2O)_{0.41}$[24] (as summarized in Figure 3f). PQ cathodes with respectable mass loadings (i.e., 3 mg cm^{-2}) also exhibited high-capacity retention over 100 cycles at 0.5 C (Figure S11, Supporting Information). Comparative studies were also conducted for other quinone-based materials, which displayed capacities considerably lower than that of PQ under the same measurement conditions (68 mAh g^{-1} for 1,4-Naphthoquinone NQ, 130 mAh g^{-1} for pyrene-4,5,9,10-tetrone PTO, see Figure S12, Supporting Information). These findings recommend PQ as a highly promising organic cathode material for CMBs.

The reaction kinetics of PQ cathodes were probed using the galvanostatic intermittent titration technique (GITT) in Figure S13 (Supporting Information). The Ca ion diffusion coefficients

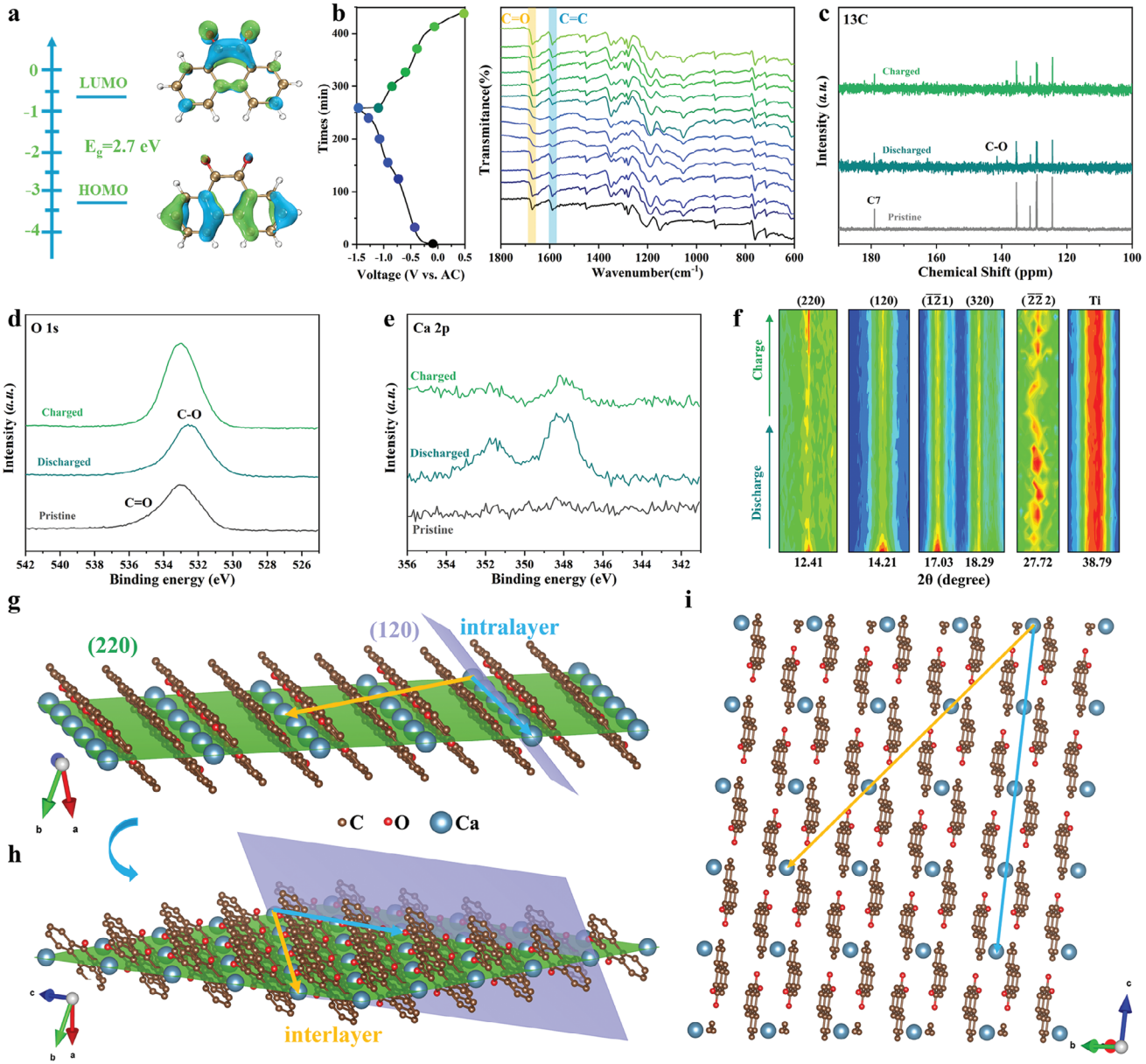

Figure 4. Ca^{2+} ions storage mechanism in PQ cathode. a) Calculated HOMO and LUMO levels of PQ, E_g is the HOMO-LUMO gap. b) ex situ FTIR spectra of PQ and the corresponding charge–discharge profile at 0.1 C, c) ^{13}C NMR, d) O1s and e) Ca 2p XPS spectra for pristine, calcinated and decalcinated PQ cathodes, f) in situ XRD pattents of PQ cycling at 0.2 C, g–i) schematic illustration of the Ca ion diffusion pathways. In (g,h), the purple plane denotes the (120) plane and the green plane for the (220) plane. The blue arrows in (i) represent the intralayer Ca^{2+} migration pathway, and the yellow arrow indicates the interlayer Ca^{2+} pathway.

(D) are in the range of 10^{-4} to 10^{-7} cm^2 s^{-1} during calciation and decalciation processes, surpassing those for other organic materials in Ca-ion batteries (i.e., 10^{-11}–10^{-8} cm^2 s^{-1} for PT,[25] 10^{-10}–10^{-8} cm^2 s^{-1} for PTCDI,[26] 10^{-8}–10^{-6} cm^2 s^{-1} for TB-COF).[11] The high Ca ion diffusion coefficient can be ascribed to the uniform alignment of carbonyl groups and weak Van der Waals π–π interactions between PQ molecules. The detailed Ca ion diffusion pathways will be interpreted later. The electronic conductivity of organic compounds is often inferred from the band gap (E_g) between the lowest unoccupied molecular orbital (LUMO, or the conduction band) and the highest occupied molecular orbital (HOMO, or the valance band) levels. In general, a smaller E_g value signifies a lower energy barrier for electron activation to the conduction band, referring to favorable electronic conductivity. The calculated E_g of 2.7 eV suggests a competent conductivity for PQ (**Figure** 4a).

To decipher the Ca ion storage mechanisms in PQ, we conducted FTIR, NMR, and X-ray photoelectron spectrometry (XPS) characterizations at different stages of calciation and decalciation. Figure 4b shows the FTIR spectra of PQ electrodes during a whole cycle with the corresponding voltage curves at 0.1 C. The characteristic peaks of C=O and C=C for pristine PQ are located

at 1681 cm^{-1} and 1591.2 cm^{-1}, respectively. During calciation, the C═O peak intensity gradually diminished corresponding to the continuous uptake of Ca^{2+} and the enolization of carbonyl groups. In the subsequent charging process, the C═O peak became strong and ultimately recovered to its pristine state. The C═C peak referring to aromatic rings remains stable throughout the reaction, indicating the robust molecular structure of PQ during enolization. The enolization reaction, C═O→C—O^-, was further verified by the appearance and subsequent disappearance of a peak at 141 ppm in the ^{13}C NMR result (Figure 4c), corresponding to the formation and cleavage of C—O bond. The O 1s and Ca 2p XPS spectra provided additional evidence of this reversible transformation (Figure 4d), with the O 1s peak shifting between 532.6 eV (C═O group) and 531.9 eV (C—O^- group) after calciation and decalciation of PQ. The Ca 2p spectra in Figure 4e directly confirmed the reversible insertion and extraction of Ca^{2+} ions in PQ.

The phase evolution of the PQ electrode during calciation and decalciation was investigated by in situ XRD. As shown in Figure 4f, no apparent new peaks for PQ are observed during Ca ions insertion and extraction. Interestingly, several XRD peaks exhibited reversible modulations in intensities during cycling at 0.2 C. In specific, the normalized XRD peak intensities, with the Ti current collector as reference (Table S3, Supporting Information), show significant attenuation of (220) and (120) planes upon full calcination, particularly a 23% reduction for the (120) plane, which partially recovered after decalciation. The other peaks, like $(\bar{1}\bar{2}1)$, (320), and (230) exhibited sustained or marginal weakening. The preservation of the brick-like morphology and dimensions of PQ after discharging and charging cycles as observed in the SEM images (Figure S14, Supporting Information) dispels the hypothesis that the intensity changes were totally attributed to the dissolution and recrystallization of PQ. The insertion of Ca^{2+} ions typically induces the lattice strain or distortion, which can alter the spacing of Bragg diffraction planes and present as shifts in XRD peak position and diffraction intensity.[27] Organic molecules, with their inherently flexible layer spacing, can mitigate these effects to some extent. However, the calciation-induced structural changes within the unit cell can affect the space group and structure amplitude, leading to the observed intensity reductions (See the details below Table S3, Supporting Information). This is supported by the subsequent restoration of diffraction intensities upon decalciation and the preservation of other peaks. Similar phenomena were also observed in XRD characterizations of organic electrodes in Mg-ion batteries and aqueous Ca-ion batteries,[25,28] suggesting the reasonability of our speculations. Furthermore, in situ Raman results in Figure S15 (Supporting Information) exhibit analogous intensity variations. The Raman peak intensity of PQ marginally diminished during calciation due to the reduced vibration of carbon atoms adjacent to the carbonyl group, and restored upon decalciation.

The spatial configurations of PQ crystal are illustrated in Figure 4g,h. It shows that the (220) plane is interposed between two ortho-carbonyl layers, while the (120) plane lies parallel to the longitudinal axis of the PQ molecule. It suggests two possible Ca^{2+} ion diffusion pathways, namely, the inter-layer transport between ortho-carbonyl groups and the intra-layer transport along the plane parallel to the PQ molecule. The efficient and rapid enolization reactions, facilitated by the transfer of Ca^{2+} ions between adjacent carbonyl groups, are enhanced by the collaborative intralayer transport in PQ. Although the intensity of other peaks decreases during calcination, the peak at 27.72° (corresponding to $\bar{2}\bar{2}2$ plane) remains consistent, which can be attributed to the T-shape π–π stacking structures of PQ with higher bonding energies (Figure S16, Supporting Information). The stable presence of $(\bar{2}\bar{2}2)$ plane suggests the robustness of PQ unit molecules. Moreover, ex situ XRD profiles of the PQ anodes were exhibited in Figure S17 (Supporting Information). During the initial cycle, the relative intensity changes in (220) and (120) planes indicate the pathways of Ca^{2+} insertion within these planes, mirroring the findings from our in situ XRD experiments. After the 50^{th} cycle, the characteristic peak of PQ persists, underscoring the robustness of the PQ crystal. Overall, these findings demonstrate the collaborative transfer of Ca^{2+} ions in PQ, which enables rapid and reversible enolization reactions to form stable enolates by ortho-carbonyl groups, achieving high-capacity and crystal integrity.

Finally, to validate the practical feasibility of the PQ cathode, a full cell was assembled using a Ca metal anode. It is noted that the Ca metal anode is irreversible in the $Ca(TFSI)_2$/TEGDME electrolyte so we prepared a compatible $Ca[B(hfip)_4]_2$ ether electrolyte for Ca metal full cells. The structural characterizations of $Ca[B(hfip)_4]_2$ are shown in Figure S18 (Supporting Information). The electrochemical performance of PQ in $Ca[B(hfip)_4]_2$/TEGDME electrolyte was initially evaluated in half-cell and full-cell configurations. Figure S19 (Supporting Information) indicates that PQ cathodes demonstrate appealing Ca^{2+} ion storage capability in half cells. Nevertheless, the poor compatibility of the Ca metal anode with TEGDME-based electrolyte significantly discouraged the reversible cycling of PQ//Ca metal full cells. To mitigate these challenges, 0.75 M $Ca[B(hfip)_4]_2$/DME electrolyte was prepared for cycling PQ in CMBs, as shown in **Figure 5a**. The $Ca[B(hfip)_4]_2$/DME electrolyte enables reversible Ca plating/stripping with low overpotentials and high reversibility (Figure S20, Supporting Information), thus it was applied to couple PQ cathodes with Ca metal into full cells.

The CV curves in Figure 5b exhibit distinct Ca ion insertion peaks consistent with these in Ca ion half cells. When cycled at a current density of 0.2 C between 0.5–3.5 V versus Ca/Ca^{2+}, the PQ//Ca metal full cell displayed a discharge capacity of 214 mAh g^{-1} with an average operating voltage of 2.5 V versus Ca/Ca^{2+} (Figure 5c). Table S4 (Supporting Information) shows that PQ//Ca full cell exhibits the highest capacity performance among the reported CMBs to date. The superior performance is attributed to the intra-layer and inter-layer channels for the rapid enolization reactions of carbonyl groups in PQ layers. Over 30 cycles, the prototype full cells consistently demonstrate distinctive discharge plateaus with reasonable capacity retentions (Figure 5d). The solubility behavior of PQ in the $Ca[B(hfip)_4]_2$/DME electrolyte is shown in Figure S21 (Supporting Information). The moderate cyclic stability of Ca metal full cells can be partially attributed to the unsatisfactory compatibility of PQ active materials in 0.75 M $Ca[B(hfip)_4]_2$/DME electrolyte (Figure S22, Supporting Information). More efforts in electrolyte modifications should be conducted to approach practical long-life CMBs.

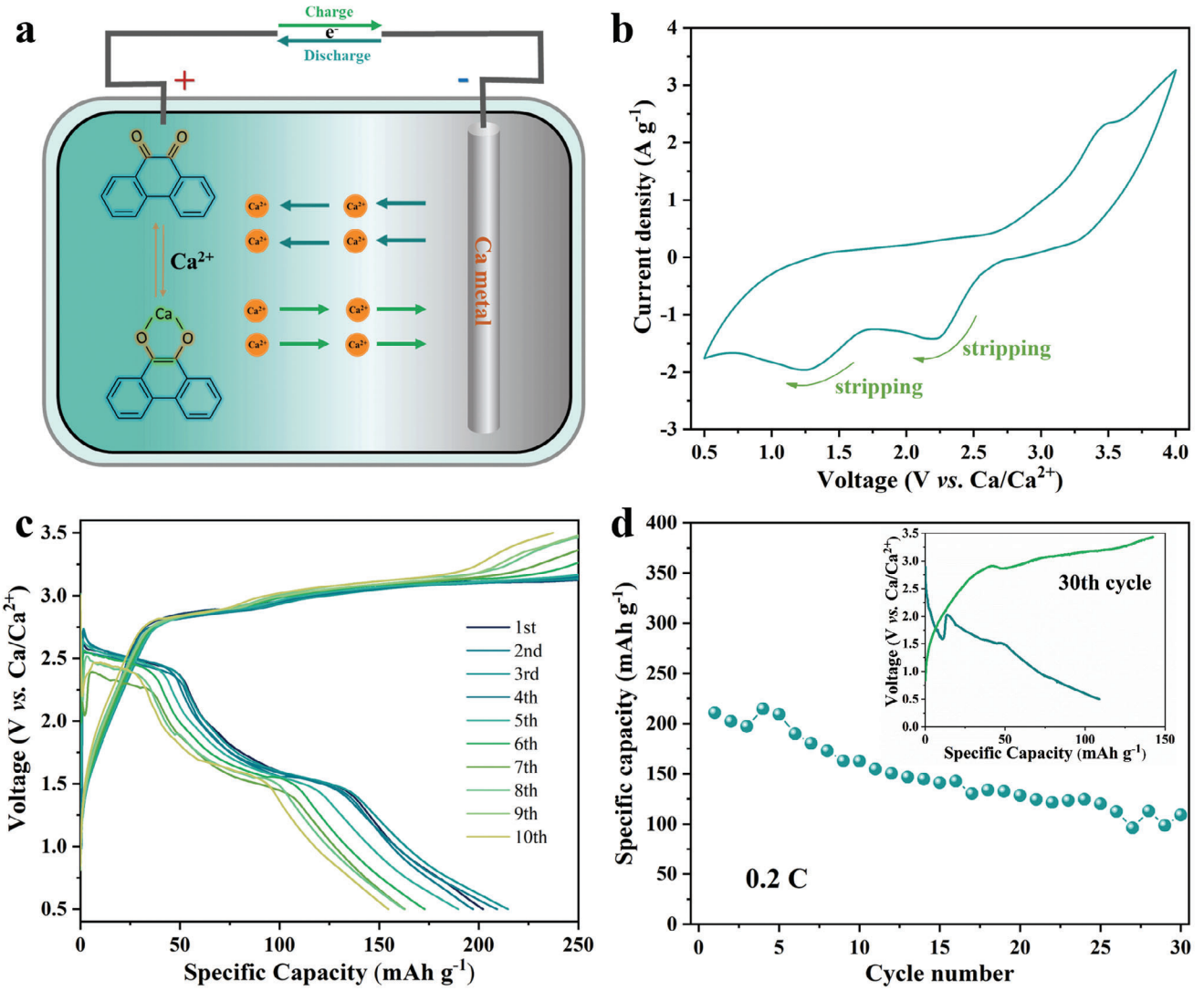

Figure 5. Electrochemical performance of Ca metal full cells. a) Schematic image of the PQ//Ca metal full cell, b) CV curve scanning at 10 mV s^{-1}, c) the initial ten cycles of discharge–charge curves, d) cyclic capacities over 30 cycles at 0.2 C. Inset of (d) shows voltage profile of the 30th cycle.

3. Conclusion

In this work, we studied a small molecular organic material as high-capacity cathodes for CMBs. The low-solubility-driven electrolytes enable the PQ cathode to deliver an unprecedently high capacity of 250 mAh g^{-1} and a theoretical energy density of 685 Wh kg^{-1}, establishing a new performance benchmark for cathodes in nonaqueous Ca ion batteries. Through a combination of dissolution analysis and DFT calculations, we unveiled that the degree of small molecule dissolution in electrolytes is contingent upon the polarity disparities, with TEGDME exhibiting the largest polarity difference from PQ and consequently the lowest dissolution propensity. It lies the foundation for high reversible capacities of PQ cathodes in Ca-ion battery systems. Comprehensive structural characterizations reveal the synergistic Ca^{2+} transport pathways through the intra-layer and inter-layer channels for the enolization reactions of carbonyl groups in PQ layers. Notably, the Ca^{2+} ion transport between adjacent carbonyl groups is conductive for efficient enolization kinetics. Benefiting from these merits, the PQ//Ca metal full cells were assembled to demonstrate remarkably high capacity. This work promotes the advancement of high-perfoprmace CMBs by unveiling the Ca ion storage behaviors in a representative PQ material in dissolution-restricted electrolyte, which heralds a new era in the development of multivalent metal batteries.

4. Experimental Section

Materials Preparation: PQ was purchased from TCI Shanghai and used without further purification. Single-walled carbon nanotubes (SWCNTs) with a length of 5–30 nm were provided by XFNANO. The solvents of DME, DEGDME, TEGDME, THF, ACN, DMAc, EC, PC, DMSO, EMC, DMC, FEC, DEC, DMF, and Hexafluoroisopropanol (HFIP) were obtained from Sigma–Aldrich and dried with molecular sieves in an Ar-filled glovebox before using. The electrolyte solutions were prepared by dissolving different molars of $Ca(TFSI)_2$ salt in above mentioned solvents. The $Ca[B(hfip)_4]_2$ salt was synthesized according to the reported receipt.[29] $Ca(BH_4)_2{\cdot}2THF$

powder (1.07 g, 5 mmol) was dissolved in 10 mL of DME. A solution of $(CF_3)_2CHOH$ (7.14 g, 42.5 mmol) was added drop by drop to the stirred solution of $Ca(BH_4)_2$. The resulting solution was stirred at room temperature for 20 h. After the reaction, the solvent was removed by vacuum drying at 40 °C overnight, followed by drying at 60 °C for 24 h, yielding 7.34 g (88%) of the $Ca[B(hfip)_4]_2$ salt. The water content of $Ca[B(hfip)_4]_2$/DME electrolyte was determined as 2.9 ppm using a Coulometric Karl Fischer titrator (Metrohm-852) under standard laboratory conditions at 25 °C. The graphene oxide (GO) interlayer was prepared by filtering GO aqueous solution on a Celgard 2400 separator. The GO aqueous solution with a concentration of 11 mg ml^{-1} was purchased from the Shanxi Coal Chemistry Research Institute. 57 µL GO aqueous solution dispersed in 5ml DI water was vacuum filtered and then dried overnight at room temperature. The areal mass loading of GO was ≈0.05 mg cm^{-2}.

Materials and Electrochemical Characterizations: The material structure was characterized by an X-ray Diffractometer (XRD, Rigaku SmartLab 9kW). The morphology and microstructure of PQ materials were characterized by Field Emission Scanning Electron Microscope (Tescan MIRA). The surface information of discharged or charged PQ was examined by XPS (Thermo Fisher Scientific Nexsa). The FTIR analyses of functional groups in PQ were conducted in BRUKER_Fourier Transform Infrared Spectroscopy with the Pike MIRacle single bounce attenuated total reflectance accessory (ATR, ZnSe IRE). NMR analyses of discharged and charged PQ were conducted in a ^{13}C NMR spectrometer. The concentration of ionic solutions in H-type cells was identified by inductively coupled plasma mass spectrometry (ICP-MS) measurements to show the shuttling of PQ through a GO-coated separator. The UV–vis absorption spectra of PQ in various electrolytes were measured by using a quartz cell in a PerkinElmer UV–vis-NIR spectrometer. All ex situ samples were carefully rinsed once with TEGDME to remove residual $Ca(TFSI)_2$ electrolytes and minimize further dissolution, followed by vacuum drying before testing. In situ, XRD measurements were performed using a Rigaku SmartLab 9 kW diffractometer equipped with Cu-Kα radiation. The experiments were conducted to monitor structural changes during the calcination and decalciation processes at a current density of 0.2 C. XRD data were collected at regular intervals of ≈10 min. In situ, Raman spectroscopy was conducted using a Witec alpha300 R spectrometer with a 633 nm laser source.

The PQ cathodes were prepared by mixing PQ powder, SWCNTs, and polytetrafluoroethylene (PTFE) in a weight ratio of 6:3:1 and then pressed on the titanium mesh current collectors for electrochemical experiments after drying at 80 °C in a vacuum oven. The mass loading of PQ cathodes (Φ = 8 mm) is ≈0.95 mg cm^{-2}. For AC anode, AC powder, and polyvinylidene fluoride (PVDF) binder were homogeneous mixed in a weight ratio of 9:1, and then N-methyl-2-pyrrolidinone (NMP) solvent was added into the mixture and stirred for 12 h to form a uniform slurry for casting on a carbon cloth substrate and dried under vacuum at 90 °C for 12 h. For full cells, Ca metal (Φ = 10 mm) was employed as the anode. CV, cyclic capacities, and GITT measurements were carried out on NEWARE battery testers.

Theoretical Calculations: All quantum chemistry calculations were performed using Gaussian 16 software. The geometries of molecules were optimized using the B3LYP exchange-correlation functional in conjunction with the basis set of 6–311++G (d, p) under the gas phase approximation. All of the optimized structures were confirmed as potential minima, with no frequency modes with imaginary eigenvalues, through frequency analyses following geometry optimizations. The LUMO and HUMO orbital energy levels and molecular electrostatic potential (MESP) were analyzed by using Multiwfn software[17] and visualized by using VMD software.

Supporting Information

Supporting Information is available from the Wiley Online Library or from the author.

Acknowledgements

This work described in this paper was fully supported by grants from the Research Grants Council of the Hong Kong Special Administrative Region, China (Project No. PolyU15305022, PolyU15304723), Department of Science and Technology of Guangdong Province (Project No. 2022A1515010206), Shenzhen Municipal Science and Technology Innovation Commission (Project No. JCYJ20220531091003008), the Research Committee of the Hong Kong Polytechnic University under project codes of 1-CD4M, 1-BBR0 and 1-45-35-YWCW.

Conflict of Interest

The authors declare no conflict of interest.

Data Availability Statement

The data that support the findings of this study are available from the corresponding author upon reasonable request.

Keywords

calcium ion batteries, electrolyte, organic cathode, small molecular electrodes

Received: July 3, 2024
Revised: October 15, 2024
Published online: October 23, 2024

[1] a) K. Kang, Y. S. Meng, J. Bréger, C. P. Grey, G. Ceder, *Science* **2006**, *311*, 977; b) F. Wu, G. Yushin, *Energy Environ. Sci.* **2017**, *10*, 435.
[2] J. W. Choi, D. Aurbach, *Nat. Rev. Mater.* **2016**, *1*, 1.
[3] a) J. Muldoon, C. B. Bucur, T. Gregory, *Chem. Rev.* **2014**, *114*, 11683; b) M. E. Arroyo-de Dompablo, A. Ponrouch, P. Johansson, M. R. Palacín, *Chem. Rev.* **2019**, *120*, 6331; c) B. Tang, L. Shan, S. Liang, J. Zhou, *Energy Environ. Sci.* **2019**, *12*, 3288; d) M.-C. Lin, M. Gong, B. Lu, Y. Wu, D.-Y. Wang, M. Guan, M. Angell, C. Chen, J. Yang, B.-J. Hwang, *Nature* **2015**, *520*, 324; e) F. Chen, Z. L. Xu, *Microstructures* **2022**, *2*, 2022012.
[4] R. J. Gummow, G. Vamvounis, M. B. Kannan, Y. He, *Adv. Mater.* **2018**, *30*, 1801702.
[5] H. Lin, J. Meng, W. Guo, R. Li, Y. Yi, Y. Ma, C. F. Cheung, D. Aurbach, Z.-L. Xu, *Energy Environ. Sci.* **2024**, *17*, 6548.
[6] Y. Hua, Y. Ma, Q. Qi, Z.-L. Xu, *Nanoscale* **2024**, *16*, 17683.
[7] a) P. A. Chando, S. Chen, J. M. Shellhamer, E. Wall, X. Wang, R. Schuarca, M. Smeu, I. D. Hosein, *Chem. Mater.* **2023**, *35*, 8371; b) X. Xu, M. Duan, Y. Yue, Q. Li, X. Zhang, L. Wu, P. Wu, B. Song, L. Mai, *ACS Energy Lett.* **2019**, *4*, 1328.
[8] a) A. L. Lipson, B. Pan, S. H. Lapidus, C. Liao, J. T. Vaughey, B. J. Ingram, *Chem. Mater.* **2015**, *27*, 8442; b) P. Padigi, G. Goncher, D. Evans, R. Solanki, *J. Power Sources* **2015**, *273*, 460.
[9] a) Z. L. Xu, J. Park, J. Wang, H. Moon, G. Yoon, J. Lim, Y. J. Ko, S. P. Cho, S. Y. Lee, K. Kang, *Nat. Commun.* **2021**, *12*, 3369; b) S. Kim, L. Yin, M. H. Lee, P. Parajuli, L. Blanc, T. T. Fister, H. Park, B. J. Kwon, B. J. Ingram, P. Zapol, R. F. Klie, K. Kang, L. F. Nazar, S. H. Lapidus, J. T. Vaughey, *ACS Energy Lett.* **2020**, *5*, 3203.
[10] J. Xie, Q. Zhang, *Small* **2019**, *15*, 1805061.
[11] S. Zhang, Y. L. Zhu, S. Ren, C. Li, X. B. Chen, Z. Li, Y. Han, Z. Shi, S. Feng, *J. Am. Chem. Soc.* **2023**, *145*, 17309.
[12] J. Bitenc, A. Scafuri, K. Pirnat, M. Lozinšek, I. Jerman, J. Grdadolnik, B. Fraisse, R. Berthelot, L. Stievano, R. Dominko, *Batteries Supercaps* **2020**, *4*, 214.
[13] B. Jiang, Y. Su, R. Liu, Z. Sun, D. Wu, *Small* **2022**, *18*, 2200049.
[14] S. Zhang, Y. Zhu, D. Wang, C. Li, Y. Han, Z. Shi, S. Feng, *Adv. Sci.* **2022**, *9*, 2200397.

[15] a) R. Rajagopalan, Y. Tang, C. Jia, X. Ji, H. Wang, *Energy Environ. Sci.* **2020**, *13*, 1568; b) Y. Lu, J. Chen, *Nat. Rev. Chem.* **2020**, *4*, 127.
[16] L. J. Riwar, N. Trapp, B. Kuhn, F. Diederich, *Angew. Chem., Int. Ed.* **2017**, *56*, 11252.
[17] T. Lu, F. Chen, *J. Comput. Chem.* **2012**, *33*, 580.
[18] P. Politzer, J. S. Murray, *ChemPhysChem* **2020**, *21*, 579.
[19] Z. Liu, T. Lu, Q. Chen, *Carbon* **2021**, *171*, 514.
[20] A. R. Katritzky, D. C. Fara, H. Yang, K. Tämm, T. Tamm, M. Karelson, *Chem. Rev.* **2004**, *104*, 175.
[21] a) F. Jing, T. Huang, G. Tao, L. Ma, D. Lu, R. Liu, X. Xi, D. Wu, *Electrochim. Acta* **2018**, *276*, 207; b) M. S. Chae, A. Nimkar, N. Shpigel, Y. Gofer, D. Aurbach, *ACS Energy Lett.* **2021**, *6*, 2659.
[22] H. Dong, O. Tutusaus, Y. Liang, Y. Zhang, Z. Lebens-Higgins, W. Yang, R. Mohtadi, Y. Yao, *Nat. Energy* **2020**, *5*, 1043.
[23] R. Dugas, J. D. Forero-Saboya, A. Ponrouch, *Chem. Mater.* **2019**, *31*, 8613.
[24] M. S. Chae, H. H. Kwak, S.-T. Hong, *ACS Appl. Energy Mater.* **2020**, *3*, 5107.
[25] C. Han, H. Li, Y. Li, J. Zhu, C. Zhi, *Nat. Commun.* **2021**, *12*, 2400.
[26] R. Li, J. Yu, F. Chen, Y. Su, K. C. Chan, Z. L. Xu, *Adv. Funct. Mater.* **2023**, *33*, 2214304.
[27] Y. Yi, Y. Xing, H. Wang, Z. Zeng, Z. Sun, R. Li, H. Lin, Y. Ma, X. Pu, M. M. Li, K. Y. Park, Z. L. Xu, *Angew. Chem., Int. Ed.* **2024**, *63*, 202317177.
[28] H. Aso, O. Tutusaus, T. S. Arthur, J. A. Kaduk, R. Mohtadi, *J. Phys. Chem. C* **2023**, *127*, 2855.
[29] Z. Li, O. Fuhr, M. Fichtner, Z. Zhao-Karger, *Energy Environ. Sci.* **2019**, *12*, 3496.